Letter

Manipulating atom-number distributions and detecting spatial distributions in lattice-confined spinor gases

J. O. Austin,[1] Z. N. Shaw,[1] Z. Chen,[1] K. W. Mahmud,[2,*] and Y. Liu[1,†]
[1]*Department of Physics, Oklahoma State University, Stillwater, Oklahoma 74078, USA*
[2]*Joint Quantum Institute, University of Maryland, College Park, Maryland 20742, USA*

(Received 18 May 2021; revised 16 August 2021; accepted 28 September 2021; published 15 October 2021)

We present an experimental study demonstrating the manipulation of atom-number distributions of spinor gases after nonequilibrium quantum quenches across superfluid to Mott-insulator phase transitions in cubic optical lattices. Our data indicate that atom distributions in individual Mott lobes can be tuned by properly designing quantum quench sequences, which suggests methods of maximizing the fraction of atoms in Mott lobes of even occupation numbers and has applications in attaining different quantum magnetic phases including massively entangled states. Spatial distributions of gases in three-dimensional lattices are derived from the observed number distributions, which reveal complex spatial dynamics during the quantum quenches. Qualitative agreements are also found between our experimental data and numerical simulations based on time-dependent Gutzwiller approximations in two-dimensional systems.

DOI: 10.1103/PhysRevA.104.L041304

Spinor Bose-Einstein condensates (BECs) in optical lattices, possessing a spin degree of freedom and tunable interactions, have been utilized to form programmable quantum simulators which are capable of studying a vast array of topics at the forefront of physics research that are too computationally complex to study using classical computers [1–11]. One feature of lattice-confined spinor gases of particular interest is that atoms in Mott-insulator (MI) lobes of different occupation numbers can have distinct properties, e.g., antiferromagnetic spinor gases can only form spin singlets in even Mott lobes [3,10–14]. Many-body spin-singlet states, consisting of massively entangled spin components, have been suggested as exemplary platforms for studying quantum memory and quantum metrology [7]. The number and spatial distributions of ultracold atoms in lattices have thus been a topic of great interest [8,15–25]. Various experimental approaches have been realized to determine these distributions after atoms are loaded into deep lattices [8,15,18,22–25]. Techniques to directly image individual lattice sites, such as quantum gas microscopy, allow for simultaneous detections of number and spatial distributions, but have thus far been highly challenging to implement in three-dimensional (3D) systems due to technical limitations, such as a short depth of focus and background contributions from nearby layers [23–25]. Indirect methods of determining number and spatial distributions are thus needed to avoid these technical challenges. A good indirect method is to identify signatures of discrete energy levels from a Fourier analysis of spin-mixing dynamics, resulting from the competition of the quadratic Zeeman energy q and the spin-dependent interaction U_2 in spinor gases [1,8]. This approach has thus far been realized only for detecting number distributions after adiabatic ramps by our previous work [8].

In this Letter, we extend this method to probe atom-number distributions after nonadiabatic quantum quenches, and more importantly we demonstrate the utilization of this method to reveal spatial distributions of atoms in 3D lattices with standard imaging systems. The derived spatial distributions of 3D lattice-confined gases indicate that atoms go through complex spatial dynamics while redistributing within a harmonic trap during the quantum quenches. Our data also confirm that atom distributions can be manipulated by properly designing quantum quench sequences, which may have important applications in attaining different many-body quantum phases. These observations suggest methods of maximizing the fraction of atoms in even Mott lobes which, among other things, may enable future works to optimize the production of massively entangled states in cold atoms. Another notable aspect of our experiment is the toolbox it provides for probing spinor atoms at the on-site level, which can be utilized to deduce the coefficients of on-site wave functions and calculate number fluctuations, the spin-singlet order parameter, and various other entanglement observables in homogeneous systems [1,7].

We apply the Bose-Hubbard (BH) model and the Gutzwiller approximation to understand the static and dynamic properties of lattice-trapped spin-1 bosons [26]. In the Gutzwiller approximation, the many-body wave function of the full lattice can be written as a product of single-site states, which for a homogeneous system of $F = 1$ atoms is $|\phi\rangle = \sum_{n_1,n_0,n_{-1}} C_{n_1,n_0,n_{-1}} |n_1, n_0, n_{-1}\rangle$ in the Fock state basis $|n_1, n_0, n_{-1}\rangle$ [4]. Here, n_{m_F} is the number of spin-m_F atoms. Fock state coefficients $P(n_1, n_0, n_{-1}) = |C_{n_1,n_0,n_{-1}}|^2$ define Fock state number distributions. The Fock state coefficient for the spin-0 component, which can be found by a Fourier analysis of the spin-mixing dynamics, is denoted

*Present address: Quidient LLC, Columbia, MD 21046.
†yingmei.liu@okstate.edu

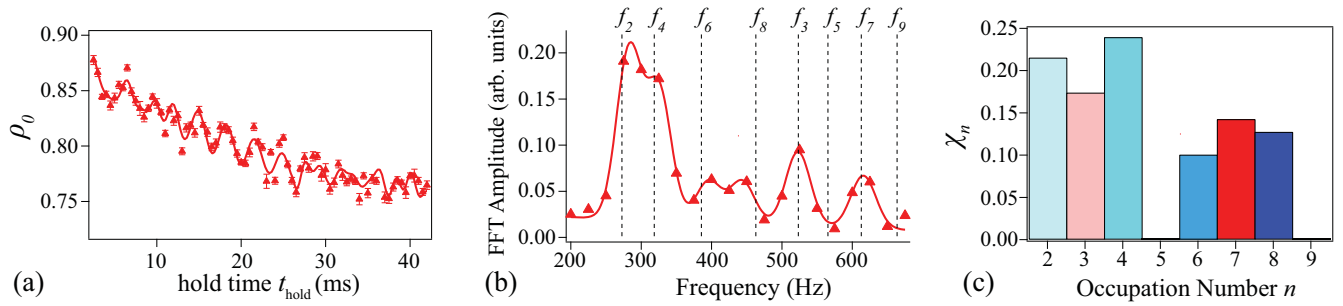

FIG. 1. (a) Observed dynamics of spin-0 atoms at $v_{\rm ramp} = 14(1)E_R/\text{ms}$ and $u_{L0} = 0E_R$. Markers represent the average of approximately 15 repeated shots at the same conditions and error bars are one standard error. The solid line is a fit based on our empirical model to guide the eye [8]. (b) Markers show FFTs over the first 40 ms of $t_{\rm hold}$ on the data shown in (a). Vertical lines mark the predicted energy signature f_n for each n, while the solid line represents Gaussian fits to each observed peak [26]. (c) Number distributions χ_n extracted from the FFT spectrum shown in (b) (see text).

as $\chi_n = \sum_{n_1,n_{-1}} |C_{n_1,n_0,n_{-1}}|^2$ [1,8]. Fock state coefficients for other spin components can be derived via the same method.

For a homogeneous system, χ_n reveals the on-site atom-number statistics which displays a Poissonian behavior in a superfluid (SF) state and gets number squeezed in the MI regime [21]. In our experimental systems, however, atoms are externally confined in a harmonic trap. This results in an inhomogeneous density profile with different atom-number statistics at individual lattice sites. In the MI state, this leads to a wedding-cake structure in the density profile with constant integer density Mott plateaus; therefore, each lattice site has different on-site number statistics. In our experiments, we collect data after releasing atoms from all trapping potentials, and each observed number distribution is thus summed over individual lattice sites i, i.e., $\chi_n = \sum_i \chi_{n_i}$.

We start each experiment cycle with a sodium spinor BEC at its SF ground state, the longitudinal polar state with $\rho_0 = 1$. Here, ρ_0 is the fractional population of spin-0 components. We then load atoms into a cubic optical lattice by adiabatically raising the lattice depth u_L to an intermediate value u_{L0} and then nonadiabatically quench u_L to a final lattice depth $u_L^{\rm final}$ at the speed $v_{\rm ramp}$ to initiate spin-mixing dynamics [26]. Because $u_L^{\rm final}$ is much deeper than the SF-MI transition points, atoms are localized into individual lattice sites by the end of the quench sequence [3]. After the lattice quench, we hold the atoms at $u_L^{\rm final}$ for a holding time $t_{\rm hold}$ before abruptly releasing them and then detect different spin components via a two-stage microwave imaging process [4,7,26].

While $q/h \lesssim 100$ Hz, spin dynamics similar to those presented in Fig. 1(a) are observed, where q is the quadratic Zeeman energy and h is Planck's constant. Consisting of multiple Rabi-type oscillations of frequencies f_n, these dynamics offer an ideal platform to probe the atom-number distributions of spinor gases [1,8]. Here, $f_n = E_n/h$ and E_n is the energy gap between the first excited state and the ground state for a fixed n [1,8]. When q and $u_L^{\rm final}$ are carefully chosen to be large enough that the frequencies of spin-mixing oscillations at individual n are well separated but q is small enough that the system displays spin oscillations after quantum quenches, the resulting spin dynamics allow us to extract the number distributions of our system. In this Letter, all data are collected at $u_L^{\rm final} = 35E_R$ and $q/h = 85$ Hz which offers a good balance between these conditions. Here, E_R is the recoil energy [4,5,8]. By conducting a fast Fourier transformation (FFT), similar to the one shown in Fig. 1(b), over the first 40 ms of each observed spin dynamics, integrating over each peak in the resulting spectrum, and dividing by the theoretical spin oscillation amplitude at each n, we can precisely determine the spectral contributions of each n [8]. The resulting normalized χ_n [see Fig. 1(c)] reflect the number distributions after the $n = 1$ Mott lobe is excluded because no spin oscillations occur when $n = 1$.

The observed atom-number distributions at various $v_{\rm ramp}$ are displayed in Fig. 2(a). Because the realizations and manipulations of some important quantum states (e.g., spin singlets) of ultracold atoms depend on the increased presence of even Mott lobes [3,10–14], one parameter of particular significance that we wish to probe is $\chi_{\rm even}$, the fraction of atoms in even Mott lobes. Figure 2(b) shows the observed $\chi_{\rm even}$ at various $v_{\rm ramp}$. The distributions found at the fastest tested speed of $v_{\rm ramp} = 54(1)E_R/\text{ms}$ have a relatively high $\chi_{\rm even}$, and there is a clear dip in $\chi_{\rm even}$ as the quench speed is lowered from $54(1)E_R/\text{ms}$ to $39(1)E_R/\text{ms}$, which then increases exponentially with $v_{\rm ramp}$ back to a relatively high $\chi_{\rm even}$ [26]. One notable result is that most observed $\chi_{\rm even}$ shown in Fig. 2(b) are significantly larger than the predicted $\chi_{\rm even}$ of 0.55 for our system of $n_{\rm peak} = 7$. Here, $n_{\rm peak}$ is the peak occupation number per lattice site in equilibrium MI states [4,5,8,26]. We find no discernible FFT spectra can be obtained after quenches at slow speeds of $v_{\rm ramp} < 10E_R/\text{ms}$ because the amplitude of spin-mixing oscillations after the quenches appears to rapidly diminish as $v_{\rm ramp}$ decreases.

We also examine the effects of varying the intermediate lattice depth u_{L0} in Fig. 2(c). In these experiments, the lattice ramp speed $v_{\rm ramp}$ is kept at $28(1)E_R/\text{ms}$ during quenches from various u_{L0} to $u_L^{\rm final} = 35E_R$. Our data in Fig. 2(c) indicate that the observed $\chi_{\rm even}$ only weakly depends on u_{L0} at this $v_{\rm ramp}$. As u_{L0} approaches SF-MI transition points, the maximum n extracted from the experimental FFT spectra appears to decrease to the predicted $n_{\rm peak}$ for equilibrium MI states, which confirms lattice ramps become more adiabatic at larger u_{L0}. In addition, while all Mott lobes of $n \leqslant n_{\rm peak}$ are observed when $u_{L0} > 0E_R$ [see Fig. 2(c)], we find that certain Mott lobes do not appear in the observed distribu-

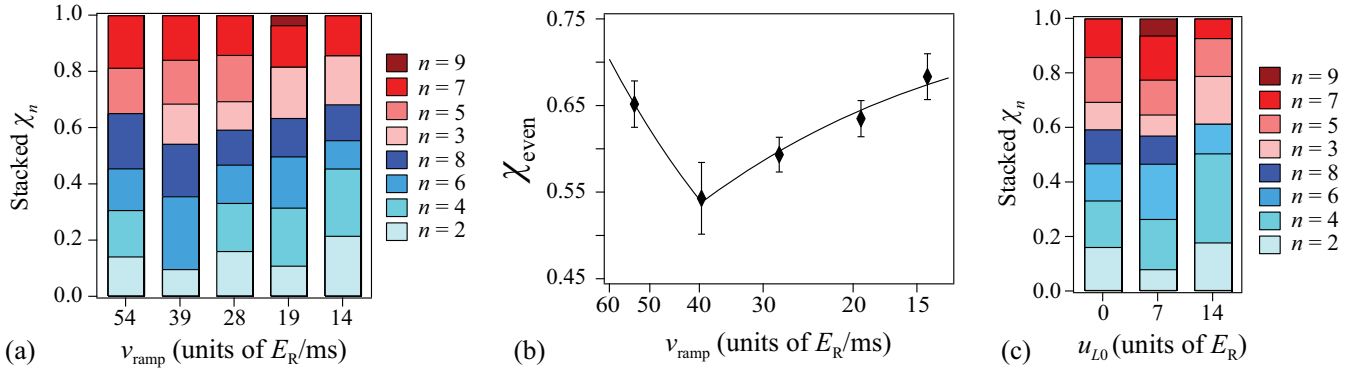

FIG. 2. (a) Observed number distributions χ_n at various $v_{\rm ramp}$ and $u_{L0} = 0E_R$. Shades of blue (red) represent even (odd) occupation numbers n with the shades getting darker as n increases from 2 to 8 (from 3 to 9). The height of each shaded box represents χ_n for a given n, while the combined height of the blue (red) boxes corresponds to the total number distribution in even (odd) Mott lobes. (b) Diamonds represent the experimentally found $\chi_{\rm even}$ for each quench sequence shown in (a). The solid line is a linear (an exponential) fit to the data when $v_{\rm ramp}$ is faster (slower) than $39(1)E_R$/ms. (c) Similar to (a) but varies u_{L0} while holding $v_{\rm ramp}$ at $28(1)E_R$/ms during the lattice ramp from u_{L0} to $35E_R$ (see text).

tions when $u_{L0} = 0E_R$, e.g., $n = 3$ at $v_{\rm ramp} = 54(1)E_R$/ms [see Fig. 2(a)]. This phenomenon may be explained by the fact that atoms are adiabatically (nonadiabatically) loaded into the 3D lattices when $u_{L0} > 0E_R$ ($u_{L0} = 0E_R$). Our observations therefore suggest that a well-designed nonadiabatic lattice ramp may be able to eliminate Mott lobes of an undesired n.

Another important feature of the observed nonequilibrium spin dynamics is they can be utilized to explore spatial distributions of 3D lattice-trapped atoms. Atoms in our inhomogeneous systems form wedding-cake structures in the MI phase with Mott lobes of higher n near the center and Mott lobes of lower n near the boundaries. As shown in Figs. 3(a)–3(c), by carefully combining the predicted wedding-cake structure and our observed atom-number distributions, spatial distributions of atoms in 3D lattices may be revealed. One interesting observation is that the extracted spatial distributions strongly depend on the lattice quench speed, i.e., more atoms locate at the trap boundaries as quenches become more adiabatic (see Fig. 3). This dependence can be quantified by examining $\chi_{2\&3}$, the fraction of atoms found in the $n = 2$ and $n = 3$ Mott lobes, versus $v_{\rm ramp}$ as seen in Fig. 3(d). The observed $\chi_{2\&3}$ appears to exponentially increase as $v_{\rm ramp}$ decreases [see the solid line in Fig. 3(d)] [26], which indicates slower lattice quenches allow atoms initially located in the trap center to have more time to flow to the trap boundaries. These findings suggest that atoms go through complex spatial dynamics while redistributing within the harmonic trap during quantum quenches providing a mechanism by which $\chi_{\rm even}$ can be manipulated.

Our experiments are performed in 3D inhomogeneous lattice-confined spin-1 spinor gases. An exact many-body simulation of such systems has not yet been reported in the literature either for equilibrium states or nonequilibrium dynamics [4]. This numerical problem is prohibitively difficult due to high Hilbert space dimensions of on-site spin-1 atoms and the inhomogeneous nature of the systems, and hence feasible theoretical simulations are limited to one and two dimensions (2D). Figure 4(a) shows typical simulation results of number distributions performed in systems similar to our experimental system but in 2D after quench sequences at various speeds and also for the initial SF ground state which corresponds to an infinitely fast ramp. Each predicted distribution shown in Fig. 4 is averaged over all lattice sites and only includes the experimentally observable Mott lobes of $n \geqslant 2$.

We find qualitative agreements between our 2D theoretical simulations and 3D experimental results, despite quantitative disparities which are expected due to the difference in

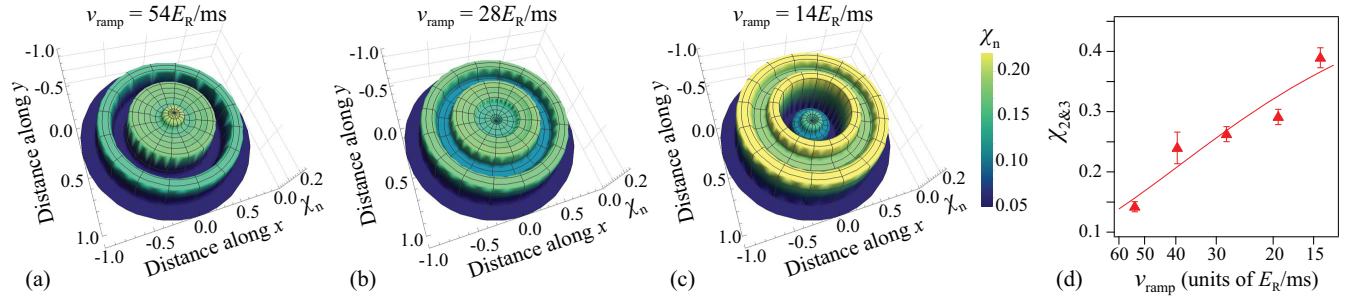

FIG. 3. (a)–(c) Spatial distributions of atoms corresponding to the measured χ_n shown in Fig. 2(a) at $v_{\rm ramp} = 54(1)$, 28(1), and $14(1)E_R$/ms, respectively (see text). The z axis and color scale correspond to the observed χ_n while the radial distance from the center denotes the predicted radii of each Mott plateau and is normalized so that the outer radius of the $n = 1$ Mott lobe is 1. (d) Markers represent the observed $\chi_{2\&3}$ from the distributions presented in Fig. 2(a). The solid line is an exponential fit.

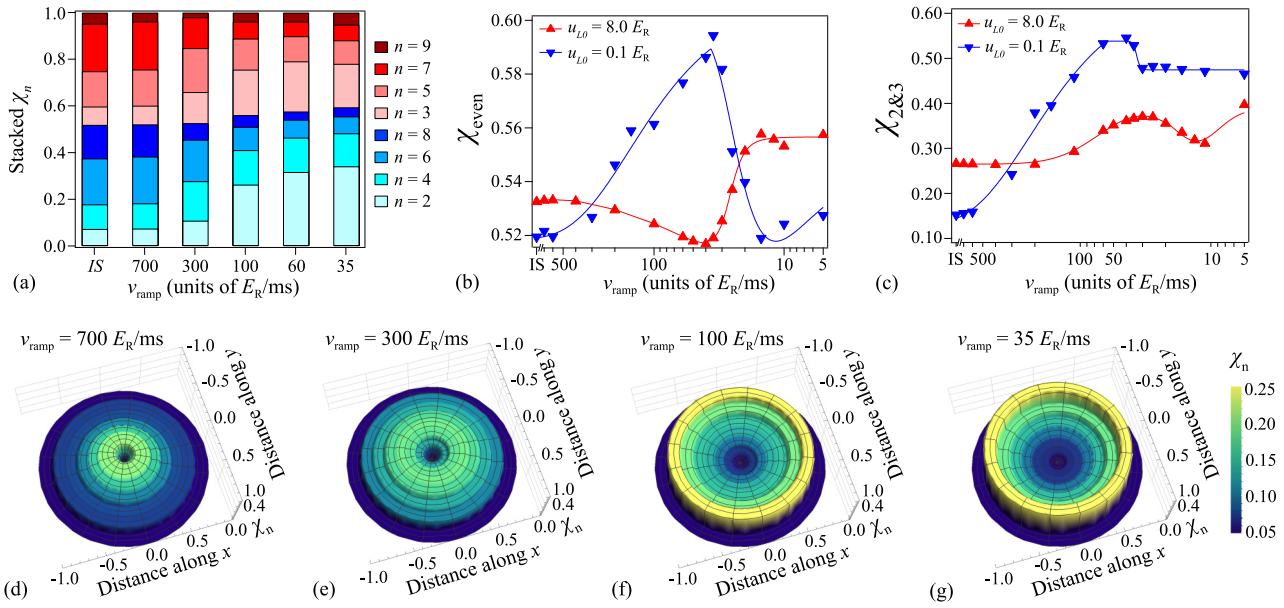

FIG. 4. (a) Predicted number distributions χ_n derived from our numerical simulations for 2D lattice-confined sodium spinor gases after ramp sequences with $u_{L0} = 0.1E_R$ at various v_{ramp} and for IS, the initial superfluid ground state. Shades of blue (red) represent even (odd) n with the shades getting darker as n increases from 2 to 8 (3 to 9). The height of each shaded box represents the predicted χ_n for a given n, while the combined height of the blue (red) boxes represents the total number distributions in even (odd) Mott lobes. (b) Markers represent fractions of even Mott lobes extracted from simulated lattice quenches similar to those shown in (a) but at various v_{ramp} and two u_{L0}. (c) Similar to (b) but markers represent $\chi_{2\&3}$. Solid lines in (b) and (c) are fitting curves to guide the eye. (d)–(g) Similar to Figs. 3(a)–3(c) but after the simulated quenches at $v_{ramp} = 700$, 300, 100, and $35E_R$/ms, respectively.

dimensionality. For example, similar to our experimental data shown in Fig. 2(a), the simulated atom-number distributions in Fig. 4(a) indicate a dependence on the lattice quench speed v_{ramp}. The predicted even fractions after simulated quenches at various v_{ramp} [see Fig. 4(b)] also display some similarities to our experimental observations illustrated in Fig. 2(b), e.g., χ_{even} exponentially increases from a value around the predicted χ_{even} for the initial SF ground state as v_{ramp} is lowered, and χ_{even} reaches its maximum at a nonadiabatic quench speed. Our theoretical results indicate that χ_{even} should decrease to the value for equilibrium MI states as v_{ramp} continues to decrease but because we are unable to observe spin oscillations at very small v_{ramp}, we have not been able to observe this experimentally. Differences between the two theory curves in Fig. 4(b) also imply that it is possible to optimize the even fraction χ_{even} by properly designing quantum quench sequences, e.g., larger maximum achievable χ_{even} may be realized at smaller u_{L0}.

Another experiment-theory similarity is the rapid increase in $\chi_{2\&3}$ as v_{ramp} is lowered [see Figs. 4(c) and 3(d)]. The differences between the two curves in Fig. 4(c) further illustrate that this effect is more prominent when the quench sequence is more nonadiabatic (i.e., when u_{L0} approaches zero). Simulated spatial distributions [see Figs. 4(d)–4(g)], corresponding to typical quenches shown in Fig. 4(a), also imply that atoms flow from the center of the trap to the boundaries as the quench speed is lowered, which qualitatively agrees with our experimental data shown in Fig. 3. These results suggest spatial distributions reach an equilibrium value when v_{ramp} is sufficiently slow to ensure the atoms initially located in the trap center have enough time to move towards the trap boundaries and equilibrate. While the nature of the redistribution for lattice trapped atoms is highly dependent on the specific model, e.g., scalar boson models would be different from the antiferromagnetic spinor models where some occupation numbers are suppressed based on U_2 and q, the effect should be present in most lattice models. Nonequilibrium spin dynamics could therefore potentially provide a convenient method to explore the spatial distribution of 3D lattice-trapped atoms with standard imaging techniques.

In conclusion, we have experimentally demonstrated atom distributions of lattice-confined spinor gases can be manipulated via quantum quenches. Our data have illustrated methods of maximizing the presence of even Mott lobes, which have applications in attaining various quantum magnetic phases including massively entangled states. This work has also suggested an indirect detection method to reveal spatial distributions of 3D lattice-confined gases with standard imaging systems. This indirect method can be applied to other atomic species and may be helpful to study intricate spatial dynamics as lattice site-resolved imaging in 3D systems is still difficult to implement. Our observations have been qualitatively described by numerical simulations using time-dependent Gutzwiller approximations in two-dimensional systems.

We thank the National Science Foundation and the Noble Foundation for financial support.

[1] K. W. Mahmud and E. Tiesinga, Dynamics of spin-1 bosons in an optical lattice: Spin mixing, quantum-phase-revival spectroscopy, and effective three-body interactions, Phys. Rev. A **88**, 023602 (2013).

[2] L. Zhao, J. Jiang, T. Tang, M. Webb, and Y. Liu, Dynamics in spinor condensates tuned by a microwave dressing field, Phys. Rev. A **89**, 023608 (2014).

[3] J. Jiang, L. Zhao, S.-T. Wang, Z. Chen, T. Tang, L.-M. Duan, and Y. Liu, First-order superfluid-to-Mott-insulator phase transitions in spinor condensates, Phys. Rev. A **93**, 063607 (2016), and references therein.

[4] J. O. Austin, Z. Chen, Z. N. Shaw, K. W. Mahmud, and Y. Liu, Quantum critical dynamics in a spinor Hubbard model quantum simulator, Commun. Phys. **4**, 61 (2021), and references therein.

[5] L. Zhao, J. Jiang, T. Tang, M. Webb, and Y. Liu, Antiferromagnetic Spinor Condensates in a Two-Dimensional Optical Lattice, Phys. Rev. Lett. **114**, 225302 (2015).

[6] N. T. Phuc, Y. Kawaguchi, and M. Ueda, Effects of thermal and quantum fluctuations on the phase diagram of a spin-1 ^{87}Rb Bose-Einstein condensate, Phys. Rev. A **84**, 043645 (2011).

[7] L. Zhao, T. Tang, Z. Chen, and Y. Liu, Lattice-induced rapid formation of spin singlets in spin-1 spinor condensates, arXiv:1801.00773.

[8] Z. Chen, T. Tang, J. Austin, Z. Shaw, L. Zhao, and Y. Liu, Quantum Quench and Nonequilibrium Dynamics in Lattice-Confined Spinor Condensates, Phys. Rev. Lett. **123**, 113002 (2019).

[9] I. Bloch, Ultracold quantum gases in optical lattices, Nat. Phys. **1**, 23 (2005).

[10] A. Imambekov, M. Lukin, and E. Demler, Spin-exchange interactions of spin-one bosons in optical lattices: Singlet, nematic, and dimerized phases, Phys. Rev. A **68**, 063602 (2003).

[11] M. Lacki, S. Paganelli, V. Ahufinger, A. Sanpera, and J. Zakrzewski, Disordered spinor Bose-Hubbard model, Phys. Rev. A **83**, 013605 (2011).

[12] E. Demler and F. Zhou, Spinor Bosonic Atoms in Optical Lattices: Symmetry Breaking and Fractionalization, Phys. Rev. Lett. **88**, 163001 (2002).

[13] M. Snoek and F. Zhou, Microscopic wave functions of spin-singlet and nematic Mott states of spin-one bosons in high-dimensional bipartite lattices, Phys. Rev. B **69**, 094410 (2004).

[14] S. K. Yip, Dimer State of Spin-1 Bosons in an Optical Lattice, Phys. Rev. Lett. **90**, 250402 (2003).

[15] R. Landig, L. Hruby, N. Dogra, M. Landini, R. Mottl, T. Donner, and T. Esslinger, Quantum phases from competing short-and long-range interactions in an optical lattice, Nature (London) **532**, 476 (2016).

[16] A. K. Tuchman, C. Orzel, A. Polkovnikov, and M. A. Kasevich, Nonequilibrium coherence dynamics of a soft boson lattice, Phys. Rev. A **74**, 051601(R) (2006).

[17] T. Zhou, K. Yang, Z. Zhu, X. Yu, S. Yang, W. Xiong, X. Zhou, X. Chen, C. Li, J. Schmiedmayer, X. Yue, and Y. Zhai, Observation of atom-number fluctuations in optical lattices via quantum collapse and revival dynamics, Phys. Rev. A **99**, 013602 (2019).

[18] S. Will, T. Best, U. Schneider, L. Hackermüller, D.-S. Lühmann, and I. Bloch, Time-resolved observation of coherent multi-body interactions in quantum phase revivals, Nature (London) **465**, 197 (2010).

[19] A. Agarwala, M. Nath, J. Lugani, K. Thyagarajan, and S. Ghosh, Fock-space exploration by angle-resolved transmission through a quantum diffraction grating of cold atoms in an optical lattice, Phys. Rev. A **85**, 063606 (2012).

[20] E. Tiesinga and P. R. Johnson, Collapse and revival dynamics of number-squeezed superfluids of ultracold atoms in optical lattices, Phys. Rev. A **83**, 063609 (2011).

[21] B. Capogrosso-Sansone, E. Kozik, N. Prokofev, and B. Svistunov, On-site number statistics of ultracold lattice bosons, Phys. Rev. A **75**, 013619 (2007).

[22] G. K. Campbell, J. Mun, M. Boyd, P. Medley, A. E. Leanhardt, L. G. Marcassa, D. E. Pritchard, and W. Ketterle, Imaging the Mott insulator shells by using atomic clock shifts, Science **313**, 649 (2006).

[23] W. S. Bakr, A. Peng, M. E. Tai, R. Ma, J. Simon, J. I. Gillen, S. Foelling, L. Pollet, and M. Greiner, Probing the superfluid-to-Mott insulator transition at the single-atom level, Science **329**, 547 (2010).

[24] P. M. Preiss, R. Ma, M. E. Tai, J. Simon, and M. Greiner, Quantum gas microscopy with spin, atom-number, and multilayer readout, Phys. Rev. A **91**, 041602(R) (2015).

[25] J. Koepsell, S. Hirthe, D. Bourgund, P. Sompet, J. Vijayan, G. Salomon, C. Gross, and I. Bloch, Robust Bilayer Charge Pumping for Spin- and Density-Resolved Quantum Gas Microscopy, Phys. Rev. Lett. **125**, 010403 (2020).

[26] See Supplemental Material at http://link.aps.org/supplemental/10.1103/PhysRevA.104.L041304 for additional details of our experimental procedures, theoretical models, and analysis methods.